Highly-oriented zirconium nitride and oxynitride coatings deposited via high-power impulse magnetron sputtering: crystal-facet driven corrosion behavior in domestic wastewater

Dr. Anna Dettlaff, Mateusz Brodowski, Marcin Kowalski, Prof. Vitezslav Stranak, Dr. Vadym Prysiazhnyi, Prof. Ewa Klugmann-Radziemska, Prof. Jacek Ryl, Prof. Robert Bogdanowicz*

Dr. A. Dettlaff, Prof. E. Klugmann-Radziemska
Gdańsk University of Technology, Faculty of Chemistry, Department of Energy Conversion and Storage,
Narutowicza 11/12, 80-233 Gdańsk, Poland
E-mail: anna.dettlaff@pg.edu.pl

M. Brodowski, M. Kowalski, Prof. R. Bogdanowicz
Gdańsk University of Technology, Faculty of Electronics, Telecommunications and Informatics, Department of Metrology and Optoelectronics,
Narutowicza 11/12, 80-233 Gdańsk, Poland

Prof. Vitezslav Stranak, Dr. Vadym Prysiazhnyi
University of South Bohemia, Institute of Physics,
Branisovska 1760, 370 05 Ceske Budejovice, Czech Republic

Prof. Jacek Ryl
Gdańsk University of Technology, Faculty of Applied Physics and Mathematics, Advanced Materials Center and Institute of Nanotechnology and Materials Engineering
Narutowicza 11/12, 80-233 Gdańsk, Poland

Keywords: high pulse magnetron sputtering, electrochemical corrosion, synthetic wastewater, linear polarization, passive layers

In the present work, highly-crystalline Zr_xN_y and $Zr_xN_yO_z$ coatings are achieved by the deposition via high-power impulse magnetron sputtering. Various N_2 and N_2/O_2 gas mixtures with argon are investigated. The chemical composition and as a result, mechanical properties of the deposited layer can be tailored along with morphological and crystallographic structural changes. The corrosion resistance behavior is studied by potentiodynamic measurements and electrochemical impedance spectroscopy in a sample of synthetic wastewater designed to imitate real-life domestic wastewater. The corrosion current density of the $Zr_xN_yO_z$ coating is in the range of 33–70 μA cm^{-2}, whereas for the zirconium nitride layers, we achieved values below 1.0 μA cm^{-2}. The highest corrosion resistance of 64 nm y^{-1} is observed for the Zr_xN_y coating deposited at an Ar/N_2 rate of 1.00 with a corrosion potential of -0.41 *vs.* Ag/AgCl.

1. Introduction

Transition metal nitrides (TMN) are ceramic materials that have attracted extensive interest because of their unusual properties such as high hardness, chemical inertness and wear resistance.[1] TMN layers are commonly applied as protective coatings against corrosion, wear, heat or scratching. Among them, zirconium nitride (Zr_xN_y) has started to attract more attention, especially in the area of coatings, due to its durability, high corrosion, thermal stability, oxidation and erosion resistance, and good electrical conductivity.[1–4] The aforementioned features depend mainly on the microstructure of the Zr_xN_y material and the corrosion products.[2,5]

Though the most common metal used is titanium, zirconium nitride has attracted some attention as it has better mechanical properties[6,7] but it also has a smaller window of deposition parameters.[8] The nitride films are typically prepared by cathodic arc deposition (better deposition rate)[9] or magnetron sputtering (better process control, better films at the nanoscale level).[10] We decided to go with a slower method as the film density played a more critical role for our current research. It has been known for decades that Zr_xN_y films exhibit good anticorrosive properties,[11–13] and some general study of comparison of nitride materials has been done.[14]

Recently, Zr_xN_y and zirconium oxynitride ($Zr_xN_yO_z$) films have been synthesized on different substrates using various techniques such as magnetron sputtering,[4,15–18] ion nitriding, plasma immersion ion implantation and deposition,[19] ion beam sputtering,[20,21] cathodic arc deposition,[5,22] plasma electrolytic oxidation,[23] and multi-arc ion plating.[24] $Zr_xN_yO_z$ has lately received attention due to its unique properties tuned by the admixture of nitrogen and oxygen during the reactive sputtering process.[25] Lin *et al*.[26] found that the electrical conductivity of $Zr_xN_yO_z$ films is controlled first by thermal activation (300–75 K) and next by Mott variable range hopping (75–10 K).

Biocorrosion studies[22,23] showed that Zr_xN_y fabricated by plasma electrolytic oxidation exhibits improved resistance to simulated body fluids. A multilayer Zr_xN_y/ZrO_2 coating effectively shielded 304 SS in a harsh artificial environment (e.g., 20 wt% HCl).[24] Next, Cubillos *et al.*[27,28] reported that $Zr_xN_yO_z$ coatings could effectively protect a stainless steel surface and form a cubic crystallographic phase. Furthermore, Wang *et al.*[29] showed that a Zr_2N_2O coating increased the corrosion resistance of 304 SS providing enhanced resistance at a transient cathodic potential attributed to the oxygen incorporation limiting anodic dissolution at high potentials.

Kiahosseini and Larijani[30] reported that corrosion resistance and adhesion could be improved by modifying the nitrogen admixture. They demonstrated that uniform and crystalline Zr_xN_y thin films could be fabricated by sputtering on biodegradable metals and alloys,[30] and further, the films were improved by substrate biasing.[31] The correlation between the concentration of N vacancies versus the corrosion resistance of Zr_xN_y films was deliberated by Pei *et al.*.[32] A relatively high content of 0.3 vacancies provided the lowest corrosion rate. Furthermore, the lowered processing pressure enhanced the hardness and corrosion inhibition as well as nitrogen vacancy incorporation. Roman *et al.*[4] reported on the high stability of Zr_xN_y coatings over a large potential range, and the dependence of the pitting potential on the deposition temperature attributed to the formation of $Zr_xN_yO_z$ and ZrO_2 phases at the top surface of the coating.

The corrosion behavior of Zr_xN_y was already extensively studied by means of potentiodynamic polarization and electrochemical impedance but mainly for bio-oriented applications conducted in simulated body fluids.[22,23]

Synthetic wastewater is a fluid revealing highly corrosive properties.[33] Furthermore, wastewater often triggers key environmental challenges in relation to water and soil pollution and the impact on biological life.[34–37] For this reason, the electrochemical oxidative treatment

of wastewater is proposed as a promising method to overcome the issues associated with its treatment.[38–41] Nevertheless, the critical limitation of the proposed approach is the limited life-time of system components (*e.g.*, tubes, reservoir, tank, *etc.*) during treatment, mainly due to pitting corrosion. Thus, Zr_xN_y is targeted for the protection of functional parts of domestic wastewater discharge systems in specific corrosive wastewater environments.

In the present work, Zr_xN_y and $Zr_xN_yO_z$ coatings were prepared by high-power impulse magnetron sputtering with different argon/nitrogen/oxygen gas ratio. The influence of the nitrogen and oxygen contents in the coatings on corrosion resistance were investigated. Surface morphology and chemical composition of these nitride and oxynitride coatings were conducted to reveal the effects inducing the electrochemical performance. To prove the capability of the proposed protective coatings, we have tested the stability of zirconium layers exposing them to an imitating real conditions of synthetic domestic wastewater. To date, there are no available detailed studies on the corrosive behavior of Zr_xN_y and $Zr_xN_yO_z$ coatings in domestic wastewater. The corrosion protection feature of zirconium nitride can lead to its potential application as potential corrosion-inhibiting coatings for protection of advanced electrodes.

2. Results and Discussion

2.1. Resistivity of zirconium nitride and oxynitride coatings

The resistivity and thickness of the deposited Zr_xN_y films was increasing with the increase of the nitrogen content in the gas admixture (see **Table 1**). There was also a difference in resistivity between the Zr_xN_y and $Zr_xN_yO_z$; the Zr_xN_y samples were conductive with resistivity in the range of 1.8 to 17.8 Ω cm, whereas the $Zr_xN_yO_z$ samples were dielectrics (resistivity $>10^6$ Ω cm), which may be related to the high content of oxygen in the layers.[42] The metallic conductivity of the Zr_xN_y films is explained by the nonvanishing DOS at the Fermi energy.[43] It was also reported that samples deposited under relatively high-flow O_2 rates result in the electronic

transport dominated by thermal activation at high temperature (>160 K)[44] due to the formation of the insulating phase with a higher band gap energy.

2.2. Nanotribology of zirconium nitride coatings

The set of samples showed excellent adhesion to the substrate and clear load-displacement curves. The calculated values of hardness and the reduced modulus of the Zr_xN_y and $Zr_xN_yO_z$ samples are presented in **Figure 1**. The hardness and reduced modulus had a clear trend towards increasing for smaller nitrogen fractions, which directly correlates with the measured resistivity and fits with the observed coloring of the deposited films (see **Figure S1**). At higher nitrogen fractions, the film changes to a dark brown color, while at lower values, it had a bright gold color typical for samples containing a high amount of Zr_xN_y bonds.[8] From the obtained data, the optimum deposition conditions to get films with better mechanical properties requires the nitrogen content to not exceed 0.8% of the total gas flow.

2.3. Morphology and composition of zirconium nitride coatings

The scanning electron microscopy (SEM) images are presented in **Figure S2**. The surface topography does not differ significantly between the zirconium nitride and oxynitride samples. The SEM results did not reveal any cracking or undulations on the studied surfaces. The coatings are homogeneous and continuous. Additionally, the morphology of samples was studied by the atomic force microscopy (AFM). The surface was relatively smooth with estimated roughness $\sigma_{RMS} \approx 0.8$ nm. This value is comparable with flat Zr_xN_y surfaces prepared by HiPIMS techniques.[45,46] The small local defects (holes) were placed randomly across the samples. They are probably induced by high energy of HiPIMS particles impinging the surface.[47] Defects concentration was low and particularly incidental, thus, they were neglected from the AFM-based roughness estimations.

The X-ray diffraction technique was used to identify the phase composition of the investigated coatings. The XRD measurements (**Figure 2**) show the successful deposition of the Zr_xN_y and $Zr_xN_yO_z$ layers. It can be seen that with the decrease of the nitrogen content during the deposition process, the diffraction peaks were more pronounced and slightly lower the value of the full width at half maximum (FWHM), particularly visible for the dominant peak observed at 56.1°. This XRD signal also testifies that the Zr_xN_y samples were preferentially oriented along the (220) plane.[4,48] The diffraction peak at $2\theta = 33.4°$ (± 0.2°) is indexed as a (111) cubic zirconium nitride phase, while at 39.0° (± 0.3°) there is a Zr_xN_y (200) plane.[44] The 6- Zr_xN_y layer exhibits an additional peak at 55.4° attributed to *m*-ZrO_2 (122).[49] Moreover, the signal intensity increased with the nitrogen flow rate, suggesting the development of crystallinity of the zirconium nitrides.

For the oxynitride samples, the signals were observed at 2θ angles of ca. 29.0°, 48.8°, 55.1° and 56.1°. The peak at $2\theta = 29.0°$ may be assigned as $Zr_xN_yO_z$ (222)[50] or *m*-ZrO_2 (111),[49] while the signal at 48.8° corresponds to $Zr_xN_yO_z$ (440)[51] (see **Figure 2B**). The results show that inside the $Zr_xN_yO_z$ samples, there is no Zr-N bonding. Furthermore, the intensity of the signal at 56.1° significantly increases in the order of 1-$Zr_xN_yO_z$, 2-$Zr_xN_yO_z$, and 3-$Zr_xN_yO_z$, suggesting the presence of a Zr_xN_y (220) plane. However, as will be shown later, for 3-$Zr_xN_yO_z$, the nitrogen content is almost absent. Thus, for the oxynitride films, the peak at 56.1° is assigned as a ZrO_2 (130) plane,[27] which shows that the layer is formed primarily by zirconium oxide instead of oxynitride. It should be noted that the diffraction signals from the nitrogen and oxygen atoms present inside the zirconia crystalline structure are very close to each other, which significantly hinders the interpretation of the results.[27] Hence, the next step was the investigation of the element composition using the X-ray photoelectron spectroscopy technique, which instead of XRD, shows only the surficial part of a sample (usually up to 5 nm).

The high-resolution spectra of zirconium (Zr 3d), nitrogen (N 1s), and oxygen (O 1s) are shown in **Figure 3**, whereas the deconvolution data are gathered in **Table 2**. The XPS survey spectra are shown in **Figure 4A,B**, while the atomic concentration of Zr, N, and O is presented in **Figure 4C,D** and was calculated from the integrated intensities of Zr $3d_{5/2}$, the N 1s, and the O 1s, respectively.

Figure 3A presents a comparison of the Zr 3d spectra of the 2-ZrN and oxynitride samples. The authors decided to present only the high-resolution XPS spectrum of the ZrN-2 sample due to the chemical similarity between the ZrN-1-6 samples. The deconvolution was done for the Zr $3d_{5/2}$ range, which can be divided into three separated peak doublets, with $Zr3d_{5/2}$ signals at 179.6 eV (Zr-N), 180.7 eV (O-Zr-N), and 181. 9 eV (Zr-O).[52,53] The N 1s spectra (**Figure 3C,F,I,L**) was decomposed into five doublets observed at 395.6 eV, 399.4 eV, and 402.9 eV attributed to N-Zr-O bonding, and two signals assigned to Zr-N bonds at 396.2 eV and 397.1 eV, respectively.[25,51,53,54] All measured samples contain a high amount of oxygen, which may be explained by post-growth ambient surface oxidation.[53,55] The reaction of zirconium oxynitride oxidation is presented in Equation (1).[28]

$$Zr_xN_yO_{z\,(s)} + \frac{2x-z}{2}O_{2\,(g)} \rightarrow xZrO_{2\,(s)} + \frac{y}{2}N_{2\,(g)} \qquad (1)$$

It should be noted that zirconium components usually have 2–5 nm thick ZrO_2 layers,[56] which match the measurement depth of the XPS technique.

The oxygen concentration in the zirconium nitride layers does not differ significantly and provides about 34 at%. For the oxynitride coating, there was a clear trend, as might have been expected. The amount of oxygen increased in the order of 1-$Zr_xN_yO_z$, 2-$Zr_xN_yO_z$, and 3-$Zr_xN_yO_z$ from 32.2 at% to 48.3 at%, as presented in detail in **Table 2**. The high content of O-Zr-O species and low amount of nitrogen in the 3-$Zr_xN_yO_z$ suggests that the dominant structure in this sample was zirconium (IV) oxide, ZrO_2. For the zirconium oxynitride samples, despite the fixed flow

of nitrogen during deposition, the nitrogen content decreased with the increase in oxygen flow. This phenomenon can be explained by the fact that from a thermodynamic point of view, Zr prefers to react with oxygen over nitrogen.[22] Moreover, the bond dissociation energy of the Zr-N bond (565 kJ mol^{-1}) is about 40% lower than the Zn-O bond (760 kJ mol^{-1})[57] inducing adatom migrations or re-etching processes.

The signal recorded in the O 1s core-level binding energy range can be deconvoluted into two peaks, placed at 529.8 and 531.6 eV, and assigned to O-Zr-O and N-Zr-O bonds, respectively, which suggest the formation of a passive layer.[25,50] Brown *et al.*[58] proposed two mechanisms of passivation reaction of Zr_xN_y coatings. In the first, the nitrogen atoms in the Zr_xN_y layer are exchanged with oxygen, leading to the formation of ZrO_2 and/or $ZrO_2{\cdot}H_2O$ as shown in Equation (2,3).[28,59] In the second mechanism, the oxygen is incorporated into the Zr_xN_y film forming an oxynitride (Zr-N-O) (Equation (4)[28]).

$$Zr_xN_{y\,(s)} + xO_{2\,(g)} \rightarrow xZrO_{2\,(s)} + \frac{y}{2}N_{2\,(g)} \quad (2)$$

$$Zr_xN_{y\,(s)} + xO_{2\,(g)} + 2xH_2O_{(l)} \rightarrow xZrO_2 \cdot 2H_2O_{(s)} + \frac{y}{2}N_{2\,(g)} \quad (3)$$

$$Zr_xN_{y\,(s)} + O_{2\,(g)} \rightarrow Zr_xN_yO_{z\,(s)} \quad (4)$$

The formation of oxynitride bonds can be seen at 180.7 eV (O-Zr-N) for the Zr $3d_{5/2}$ spectrum, at 395.6 eV, 399.4 eV, and 402.9 eV (N-Zr-O) for the N 1s spectrum, and analogously for the O 1s spectrum at 531.6 eV (N-Zr-O). According to the O 1s and N 1 s spectra, the amount of N-Zr-O increased along the Zr_xN_y sequence 7- Zr_xN_y < 5-Zr_xN_y < 3-Zr_xN_y < 2-Zr_xN_y, see Table 2. In the same sequence, a decrease of O-Zr-O bonds can be seen. Similarly to the zirconium nitride samples, with the increasing oxygen flow during the deposition of the $Zr_xN_yO_z$, the number of N-Zr-O bonds decreased at the expense of Zr-O bonds.

2.4. Corrosion tests of zirconium nitride coatings

2.4.1. Results of electrochemical impedance spectroscopy studies

Electrochemical impedance spectroscopy (EIS) and linear polarization (CP) were employed to investigate the corrosion characteristics of the Zr_xN_y and $Zr_xN_yO_z$ layers. The recorded EIS impedance spectra are presented in the form of Nyquist and Bode plots and are shown in **Figure 5** and **Figure S3**, respectively. The collected impedance data were approximated by an electric equivalent circuit (EEQC), using the ZSimpWin analyser. The values of each electrical parameter estimated using the aforementioned EEQC are gathered in **Table 3**.

The proposed EEQC consists of two time constants and corresponds to the two layers: passive layer and coating (**Figure 6**). In this model, the resistor R_e corresponds to the electrolyte resistance, R_f denotes the passive film resistance,[60,61] C_1 is the corrosion capacitance of the coating, whereas R_{ct} is attributed to the charge-transfer resistance. The CPE is the Constant Phase Element and represents the quasi-capacitance of the double layer. The CPE impedance is defined as $Z_{CPE} = 1/Q(j\omega)^n$, where Q is the quasi-capacitive parameter, n is the CPE exponent, which corresponds to the system homogeneity ($0 \leq n \leq 1$), for n tending to 1, CPE represents an ideal, homogeneous capacitor, j reveals the imaginary unit, and ω displays the angular frequency.

The value of polarization resistance R_p is directly related to corrosion resistance – R_p is inversely proportional to the corrosion rate. Thus, the larger the R_p value, the better the corrosion resistance.[61–63] The polarization resistance is the sum of R_{ct} and R_f, however, due to the significant difference of units between these resistances, it can be assumed that R_{ct} determines the R_p value. According to the EIS results (**Figure 5**), the samples with the greatest number of N-Zr-O bonds, 1-Zr_xN_y and 2-Zr_xN_y, show the best corrosion resistance, with R_{ct} equal to 92.9 and 68.0 MΩ cm^2, respectively.

There is a significant difference in the charge transfer resistance between the zirconium nitride and zirconium oxynitride layers. The degradation process at the interface of the Zr_xN_y and the

domestic wastewater was more sluggish than that of the $Zr_xN_yO_z$. All of the $Zr_xN_yO_z$ samples showed R_{ct} values below 7.07 MΩ·cm^2, which may be associated with the low number of nitrogen atom inside the layers. Referring to literature,[42] the layer of oxynitride, which is surprisingly thicker in the Zr_xN_y coatings, is highly stable in aggressive environments due to the formation of ZrO_2 on the coating's surface, as shown in Equation (5):

$$ZrN_xO_y + zH_2O \rightarrow \frac{y+z}{2}ZrO_2 + \frac{x}{2}N_2 + zH_2 \quad (5)$$

Moreover, the parameter *n* for the $Zr_xN_yO_z$ is lower (0.74–0.81) than for the ZrN samples (0.88–0.91), which indicates the appearance of the frequency dispersion of the capacitance due to the considerably higher level of surface electric heterogeneity of these samples.

2.4.2. Results of linear polarization studies

Based on the extrapolation of the linear polarization curves (see **Figure 7**), recorded in the range of the low overpotentials, we estimated corrosion current density j_{corr} and corrosion potential E_{corr}. The results are gathered in **Table 4**. Further, the comparison of the polarization resistance and current densities is presented in **Figure 8**.

Two of the three different $Zr_xN_yO_z$ coatings exhibited higher a corrosion potential value regarding the Zr_xN_y coatings, a feature connected with surface coverage by ZrO_2. Importantly, the corrosion rate occurring at the Zr_xN_y surface is anodically-controlled, while the $Zr_xN_yO_z$ coatings are characterized by a mixed type of control. These results suggest, that oxidizing the Zr_xN_y coating surface does not restrict the anodic oxidation, as would be expected from any sample covered with the protective passive layer. These observations could be explained by the peeling-off of the ZrO_2 coatings neglecting their protective behavior, as was noted in corrosion tests by other authors.[24] A partially peeled-off passive layer would not improve the corrosion resistance; on the contrary, it would increase the corrosion rate due to the possible formation of

active-passive galvanic microcells. The decrease in surface homogeneity is confirmed by the drop of the CPE exponent within the impedance studies.

The corrosion current density of the $Zr_xN_yO_z$ coating was in the range of 33–70 μA cm^{-2}, whereas for the zirconium nitride layers, the j_{corr} value was below 1.0 μA cm^{-2}. The corrosion potential of the 1-$Zr_xN_yO_z$ and 2-$Zr_xN_yO_z$ coating shifted to the positive potentials and reached *ca.* 0.12 V (*vs.* Ag/AgCl). On the contrary, the 3-$Zr_xN_yO_z$ sample showed negative potential (-0.36 V). The difference is due to the different concentrations of nitrogen and oxygen atoms showed in the XPS results. The 3-$Zr_xN_yO_z$ may be considered as zirconium oxide, not zirconium oxynitride due to negligible amount of nitrogen.

The linear polarization results significantly coincide with the EIS results. The best corrosion resistance can be seen for the 2-Zr_xN_y (64 nm y^{-1}), followed by the 1-Zr_xN_y (80 nm y^{-1}). The same trend is observed analysing the R_p values, the samples synthesized with a higher nitrogen content in the $Ar/N_2/O_2$ mixture flow show better anti-corrosion properties. The high corrosion resistance of Zr_xN_y coatings can be attributed to their ability to produce a passive layer, not by metal nitride coating.[64] Moreover, at the interface of the coating with the aqueous electrolyte, a layer of hydrated zirconia oxygen forms, which cuts off contact of the aggressively corrosive environment from the sample.

The presence of passivation was also justified by the XPS results. The best corrosion resistance was shown by the Zr_xN_y samples with the higher number of N-Zr-O bonds at the expense of O-Zr-O bonds; namely 1-Zr_xN_y and 2-Zr_xN_y.

The zirconium oxynitride layers exhibited worse corrosion behavior than the Zr_xN_y samples. The corrosion rate of the zirconium oxynitrides was much higher and reached 8.5 μm y^{-1} for the 2-$Zr_xN_yO_z$ layer. Furthermore, the layer should be homogeneous. According to the EIS

results, the *n* parameter of the oxynitride was lower than 0.81, which suggests greater heterogeneity, which may influence the corrosion properties.

The electrochemical corrosion behavior of the films deposited by magnetron sputtering was mainly affected by three material properties: (i) composition, (ii) morphology, and (iii) architecture. These characteristics were, in turn, affected by intrinsic and extrinsic features of the system substrate-film-electrolyte, such as the type of film growth, defects, density, phases, resistivity, and film-substrate adhesion, among others. As a result, the great difficulty of controlling the electrochemical corrosion of magnetron-sputtered films lays in the fact that some of these features are interconnected, and thus, by changing one, the others will be modified. For example, the composition of the films (together with the deposition conditions) can largely alter their columnar or granular growth, as well as the porosity and boundary density in the materials. Changing the architecture of the coatings by creating bi-layers or multilayers may alter the porosity and defects of the system, also affecting the electrochemical corrosion. Moreover, the type of substrate not only modifies the growth of the films, but also activates galvanic processes within the films and/or alters their adhesion strength.

3. Conclusion

We present highly-crystalline Zr_xN_y and $Zr_xN_yO_z$ coatings formed by high-power impulse magnetron sputtering (HiPIMS) in an atmosphere containing argon with various N_2, and N_2/O_2 gas admixtures.

The nanotribology tests revealed better mechanical properties of the coatings deposited with low nitrogen content, which optimally should not exceed 0.8% to maintain high coating hardness above 24.5 GPa. Similarly, the O_2 content significantly reduces the coating hardness. The differences emerge from the alteration of the coatings' chemistry and structure. The XRD studies allowed us to conclude the preferential orientation of Zr_xN_y crystallites along the (220)

plane. On the other hand, the oxynitride samples had a more diversified crystallographic structure, which was due to the formation of ZrO_2 oxides at the coating surface, further testified with the XPS.

Next, we successfully conducted corrosion resistance tests using polarization studies and electrochemical impedance spectroscopy for each investigated coating in a synthetic wastewater. The Zr_xN_y coatings offer outstanding anti-corrosion properties in the investigated corrosive media, which are as low as 64 nm/year in the case of a 2-ZrN sample (1.00% N_2). This effect is obtained while maintaining a sample resistivity of 6 Ω cm. The N_2 concentration during the HiPIMS coating formation has a limited influence on the deterioration of the remarkable anti-corrosion properties of the Zr_xN_y coatings, however, a slow corrosion rate increase with the N_2 concentration decrease was observed. In contrast, despite the presence of a zirconia oxide passive film, the estimated $Zr_xN_yO_z$ coating's corrosion rate is over three orders of magnitude higher, reaching a maximum of 8.5 μm $year^{-1}$ (0.98% N_2, 0.69% O_2). This is an effect which was concluded to be most likely due to the higher heterogeneity of the deposited coating, as testified by the capacitance dispersion effect in the impedance study.

In conclusion, our findings provide proof that the deposited Zr_xN_y coatings with approximately 0.83–1.00% N_2 content in the gas mixture offer the best combination of both mechanical properties and corrosion resistance in domestic wastewater.

4. Experimental Section

Chemicals

All reagents were analytical grade and used without further purification.

Zirconium nitride coating fabrication

The Zr_xN_y and $Zr_xN_yO_z$ films were deposited using reactive magnetron sputtering onto silicon (111) substrates (see **Figure 9A**). A planar magnetron (3-inch magnetron with 99.999% Zr target) powered by high-power impulse magnetron sputtering – HiPIMS (pulse duration was varied from 70 μs to 100 μs with a 100 Hz repetition rate to stabilize the discharge) in an $Ar/N_2/O_2$ atmosphere; more in detail described elsewhere.[65,66] Depending on the ratio between the gases, and the resultant chemical composition, the mechanical properties of the deposited layer could be tailored.[67] The specified preparation conditions are gathered in **Table 5**. The optimized deposition conditions were as follows: 0.6 Pa pressure, 10 cm sample-to-magnetron distance. The varied parameter was the ratios of nitrogen, argon, and oxygen. The Zr_xN_y samples were prepared for 30 min without oxygen flow. The argon flow (99.999%) was changed from 90 sccm to 20 sccm, and the nitrogen flow (99.999%) was fixed to 0.5 sccm. The DC powering the HiPIMS was fixed to 400 mA, while the voltage was increased from 530 V to 600 V with the Ar varying from 40 sccm to 90 sccm, respectively. The ZrO_xN_y coatings were deposited for 60 min with an additional oxygen (99.99%) flow. For these samples, argon flow was fixed to 0.5 sccm, whereas the Ar flow was 50 sccm.

Domestic wastewater preparation

The synthetic wastewater was prepared according to the composition presented in Table S1.

Characterization techniques

The surface morphology of the zirconium nitride coatings was studied using a Thermo Fischer Phenom XL scanning electron microscope (SEM) with an integrated energy dispersive x-ray spectrometer. The phase composition was characterized by X-ray diffraction (XRD) with regard to line position, intensity, and line profile of the observed Bragg reflections. The XRD was performed on a D8 ADVANCE diffractometer (Bruker AXS) with Cu Kα radiation (40 kV, 40 mA) in the 2θ range up to 80° at incidence angle ω = 1°.

The chemical composition of the Zr_xN_y and $Zr_xN_yO_z$ layers was investigated by X-ray photoelectron spectroscopy (XPS) using an Axis Supra spectrometer (Kratos Analytical) with a monochromatic Al Kα X-ray source. The pass energy was selected to be 10 eV. After subtracting the background signal, the spectra were fitted by mixed Gaussian-Lorentzian functions.

The mechanical properties of the deposited structures were tested using a NanoTest instrument (Wales) equipped with a diamond Berkovich indenter under the following conditions: a normal load of 4 mN at a loading/unloading rate of 0.4 mN s^{-1}, 10 s creep period was set. The calculations of hardness H and reduced elastic modulus Er were performed using standard procedure.[68] The thickness of the coating (determined from a step profile on the partially covered samples) was measured by Tencor Instruments Alpha-Step 500 profilometer (USA). Measurement was done as average from at least three points on each sample.

The electrochemical studies were performed using a VMP-300 Bio-Logic potentiostat–galvanostat (France) in the EC-Lab software. The three-electrode assembly was used. The $Zr_xN_yO_z$ coatings, deposited on silicon, were used as the working electrodes (geometric area *ca*. 0.2 cm^2). A Pt mesh served as the counter electrode, while an Ag/AgCl wire and an Ag/AgCl 3.0_M KCl electrode were the reference electrodes (see **Figure 9B**). The electrochemical impedance spectroscopy (EIS) was carried out in a wide frequency range from 5 mHz to 100 kHz in a synthetic wasterwater solution with a peak-to-peak amplitude of 10 mV and 6 points per frequency decade. The EIS spectra were recorded in potentiostatic polarization mode at corrosion potential E_{corr}. Linear polarization (LP) was conducted in a domestic wastewater solution in the polarization range between ±0.25 V vs. E_{corr} with the scan rate equal to 1 mV s^{-1}. Prior to the EIS and LP measurements, each sample was initially conditioned for 15 min. Corrosion rate V_{corr} (mm y^{-1}) was calculated according to the Equation (6).[69,70]

$$V_{corr} = \frac{I_{corr} \cdot K \cdot E_w}{d \cdot A}, \quad (6)$$

where K is a constant equal to 3272, E_w is the equivalent weight, d is the material density, and A is the geometric surface area. The E_w value was determined as the ratio of the molar mass of the compound to be reacted to the number of electrons exchanged in the reaction. The mass of the Zr_xN_y layer, considerably simplified, was assumed to be 119.23 g mol^{-1}. The number of electrons exchanged was taken to be equal to 4, taking into account the considerations on the thermodynamic stability between Z_xN_y and $ZrO_2 \cdot 2H_2O$ shown by Alias.[71] However, the actual reactions taking place during this the process can be much more complex, as discussed later in this publication. It should be noted that values determined in this way are more indicative and serve more to compare the anti-corrosion properties of samples than to give exact values of the corrosion rate.

Supporting Information

Supporting Information is available from the Wiley Online Library.

Acknowledgements

This work was supported by the European Economic Area and Norway Grants (grant no. NOR/POLNOR/i-CLARE/0038/2019-00). The DS funds of the Faculty of Electronics, Telecommunications, and Informatics of the Gdansk University of Technology are also acknowledged.

Received: ((will be filled in by the editorial staff))
Revised: ((will be filled in by the editorial staff))
Published online: ((will be filled in by the editorial staff))

References

[1] C. P. Ferreira, M. das M. R. de Castro, E. K. Tentardini, V. de F. C. Lins, P. A. Saliba, *Surf. Eng.* **2018**, *0*, 1.

[2] J. Xu, S. Xu, P. Munroe, Z. H. Xie, *RSC Adv.* **2015**, *5*, 67348.

[3] V. Pejaković, V. Totolin, H. Göcerler, J. Brenner, M. Rodríguez Ripoll, *Tribol. Int.* **2014**, *91*, 267.

[4] D. Roman, J. Bernardi, C. L. G. De Amorim, F. S. De Souza, A. Spinelli, C. Giacomelli, C. A. Figueroa, I. J. R. Baumvol, R. L. O. Basso, *Mater. Chem. Phys.* **2011**, *130*, 147.

[5] Q. G. Zhou, X. D. Bai, Y. H. Ling, D. Q. Peng, J. Xu, D. R. Wang, *J. Mater. Sci.* **2005**, *40*, 2733.

[6] M. Valikhani, S. Chandrashekhar, *Int. J. Adv. Manuf. Technol.* **1987**, *2*, 75.

[7] S. Chandrashekhar, S. Chatterjee, M. Gaiser, *Int. J. Prod. Res.* **1990**, *28*, 1759.

[8] M. Nose, M. Zhou, E. Honbo, M. Yokota, S. Saji, *Surf. Coatings Technol.* **2001**, *142–144*, 211.

[9] D. F. Arias, Y. C. Arango, A. Devia, *Study of TiN and ZrN thin films grown by cathodic arc technique*, Vol. 253, **2006**, pp. 1683–1690.

[10] J. V. Ramana, S. Kumar, C. David, A. K. Ray, V. S. Raju, *Mater. Lett.* **2000**, *43*, 73.

[11] E. Budke, J. Krempel-Hesse, H. Maidhof, H. Schüssler, *Surf. Coatings Technol.* **1999**, *112*, 108.

[12] U. K. Wiiala, I. M. Penttinen, A. S. Korhonen, J. Aromaa, E. Ristolainen, *Surf. Coatings Technol.* **1990**, *41*, 191.

[13] W. J. Chou, G. P. Yu, J. H. Huang, *Surf. Coatings Technol.* **2003**, *167*, 59.

[14] I. Milošev, H. H. Strehblow, B. Navinšek, *Thin Solid Films* **1997**, *303*, 246.

[15] S. Ningshen, R. K. Gupta, S. Kamal, V. Chawla, R. Chandra, U. K. Mudali, *Surf. Eng.* **2013**, *29*, 264.

[16] A. Poulon-Quintin, C. Faure, L. Teulé-Gay, J. P. Manaud, *Thin Solid Films* **2010**, *519*, 1600.

[17] N. Farkas, G. Zhang, R. D. Ramsier, E. A. Evans, J. A. Dagata, *J. Vac. Sci. Technol. A Vacuum, Surfaces, Film.* **2008**, *26*, 297.

[18] D. D. Kumar, G. S. Kaliaraj, *J. Mech. Behav. Biomed. Mater.* **2018**, *77*, 106.

[19] Y. Cheng, Y. F. Zheng, *IEEE Trans. Plasma Sci.* **2006**, *34*, 1105.

[20] M. M. Larijani, M. Elmi, M. Yari, M. Ghoranneviss, P. Balashabadi, A. Shokouhy, *Surf. Coatings Technol.* **2009**, *203*, 2591.

[21] I. Milošev, H. H. Strehblow, M. Gaberšček, B. Navinšek, *Surf. Interface Anal.* **1996**, *24*, 448.

[22] Y. Xin, C. Liu, K. Huo, G. Tang, X. Tian, P. K. Chu, *Surf. Coatings Technol.* **2009**, *203*, 2554.

[23] C. H. Hsiao, H. P. Teng, F. H. Lu, *Surf. Coatings Technol.* **2015**, *269*, 295.

[24] Z. Lei, Q. Zhang, X. Zhu, D. Ma, F. Ma, Z. Song, Y. Q. Fu, *Appl. Surf. Sci.* **2018**, *431*, 170.

[25] Y. Yuan, R. Lan, C. Yan, R. Liu, *Mod. Phys. Lett. B* **2018**, *32*, 1.

[26] Z. Lin, G. Zhan, X. Li, M. You, Y. Zeng, F. Wang, J. Liu, *Semicond. Sci. Technol.* **2019**, *34*.

[27] G. I. Cubillos, M. Bethencourt, J. J. Olaya, *Appl. Surf. Sci.* **2015**, *327*, 288.

[28] G. I. Cubillos, E. Romero, J. E. Alfonso, *Mater. Chem. Phys.* **2016**, *176*, 167.

[29] X. Z. Wang, H. Luo, T. Muneshwar, H. Q. Fan, K. Cadien, J. L. Luo, *ACS Appl. Mater. Interfaces* **2018**, *10*, 40111.

[30] S. R. Kiahosseini, M. Mojtahedzadeh Larijani, *Appl. Phys. A Mater. Sci. Process.* **2017**, *123*, 0.

[31] M. Azibi, N. Saoula, H. Aknouche, *J. Electr. Eng.* **2019**, *70*, 112.

[32] C. Pei, L. Deng, H. Liu, Z. He, C. Xiang, S. Zhang, D. Sun, *Vacuum* **2019**, *162*, 28.

[33] S. Fudala-Ksiazek, M. Sobaszek, A. Luczkiewicz, A. Pieczynska, A. Ofiarska, A. Fiszka-Borzyszkowska, M. Sawczak, M. Ficek, R. Bogdanowicz, E. M. Siedlecka, *Chem. Eng. J.* **2018**, *334*, 1074.

[34] M. Morozesk, M. M. Bonomo, I. da C. Souza, L. D. Rocha, I. D. Duarte, I. O. Martins,

L. B. Dobbss, M. T. W. D. Carneiro, M. N. Fernandes, S. T. Matsumoto, *Chemosphere* **2017**, *184*, 309.

[35] J. Cui, F. Li, Y. Wang, Q. Zhang, W. Ma, C. Huang, *Sep. Purif. Technol.* **2020**, *250*, 117116.

[36] M. Zhang, W. Ma, J. Cui, S. Wu, J. Han, Y. Zou, C. Huang, *J. Hazard. Mater.* **2020**, *383*, 121152.

[37] M. Zhang, W. Ma, S. Wu, G. Tang, J. Cui, Q. Zhang, F. Chen, R. Xiong, C. Huang, *J. Colloid Interface Sci.* **2019**, *547*, 136.

[38] E. Kattel, A. Kivi, K. Klein, T. Tenno, N. Dulova, M. Trapido, *Desalin. Water Treat.* **2016**, *57*, 13236.

[39] S. M. Iskander, B. Brazil, J. T. Novak, Z. He, *Bioresour. Technol.* **2016**, *201*, 347.

[40] M. Pierpaoli, P. Jakobczyk, M. Sawczak, A. Łuczkiewicz, S. Fudala-Książek, R. Bogdanowicz, *J. Hazard. Mater.* **2021**, *401*, 123407.

[41] M. Pierpaoli, M. Szopińska, B. K. Wilk, M. Sobaszek, A. Łuczkiewicz, R. Bogdanowicz, S. Fudala-Książek, *J. Hazard. Mater.* **2021**, *403*.

[42] X. Z. Wang, T. P. Muneshwar, H. Q. Fan, K. Cadien, J. L. Luo, *J. Power Sources* **2018**, *397*, 32.

[43] I. Milosev, H. H. Strehblow, B. Navinšek, *Thin Solid Films* **1997**, *303*, 246.

[44] G. Zhan, J. Liu, J. Guo, J. Feng, B. Xu, B. Yang, X. Chen, C. Yang, *J. Mater. Sci. Mater. Electron.* **2015**, *26*, 9188.

[45] Y. P. Purandare, A. P. Ehiasarian, P. E. Hovsepian, *J. Vac. Sci. Technol. A Vacuum, Surfaces, Film.* **2011**, *29*, 011004.

[46] T. Kuznetsova, V. Lapitskaya, A. Khabarava, S. Chizhik, B. Warcholinski, A. Gilewicz, *Appl. Surf. Sci.* **2020**, *522*, 146508.

[47] S. Severin, M. Naveed, S. Weiß, *Adv. Mater. Sci. Eng.* **2017**, 1.

[48] B. Warcholinski, A. Gilewicz, A. S. Kuprin, G. N. Tolmachova, V. D. Ovcharenko, T.

A. Kuznetsova, V. A. Lapitskaya, S. A. Chizhik, *J. Frict. Wear* **2019**, *40*, 163.

[49] G. I. Cubillos, J. J. Olaya, M. Bethencourt, G. Cifredo, G. Blanco, *Rev. Mex. Fis.* **2014**, *60*, 233.

[50] G. I. Cubillos, J. J. Olaya, M. Bethencourt, G. Antorrena, K. El Amrani, *Mater. Chem. Phys.* **2013**, *141*, 42.

[51] A. Rizzo, M. A. Signore, L. Mirenghi, E. Piscopiello, L. Tapfer, *J. Phys. D. Appl. Phys.* **2009**, *42*.

[52] Y. Yuan, J. Wang, S. Adimi, H. Shen, T. Thomas, R. Ma, J. P. Attfield, M. Yang, *Nat. Mater.* **2019**.

[53] T. Muneshwar, K. Cadien, *Appl. Surf. Sci.* **2018**, *435*, 367.

[54] K. C. Han, G. Q. Lin, C. Dong, K. P. Tai, X. Jiang, *Acta Metall. Sin. (English Lett.* **2017**, *30*, 1100.

[55] M. Ritala, E. Rauhala, *J. Electrochem. Soc.* **1995**, *142*, 2731.

[56] T. R. Allen, R. J. M. Konings, A. T. Motta, *Compr. Nucl. Mater.* **2012**, *5*, 49.

[57] J. Speight, *Lange's Handbook of Chemistry*, McGraw-Hill Professional, **2004**.

[58] R. Brown, M. N. Alias, R. Fontana, *Surf. Coatings Technol.* **1993**, *62*, 467.

[59] M. Geng, G. He, Z. Sun, J. Chen, Z. Yang, Y. Li, *Coatings* **2018**, *8*.

[60] P. M. Samim, A. Fattah-Alhosseini, H. Elmkhah, O. Imantalab, *Mater. Res. Express* **2019**, *6*, 0.

[61] B. Ramezanzadeh, S. Y. Arman, M. Mehdipour, B. P. Markhali, *Appl. Surf. Sci.* **2014**, *289*, 129.

[62] P. M. Samim, A. Fattah-Alhosseini, H. Elmkhah, O. Imantalab, *Mater. Res. Express* **2019**, *6*, 0.

[63] P. Yi, L. Zhu, C. Dong, K. Xiao, *Surf. Coatings Technol.* **2019**, *363*, 198.

[64] S. Ningshen, R. K. Gupta, S. Kamal, V. Chawla, R. Chandra, U. K. Mudali, *Surf. Eng.* **2013**, *29*, 264.

[65] M. Čada, P. Adámek, V. Straňák, Š. Kment, J. Olejníček, Z. Hubička, R. Hippler, *Thin Solid Films* **2013**, *549*, 177.

[66] V. Stranak, H. Wulff, P. Ksirova, C. Zietz, S. Drache, M. Cada, Z. Hubicka, R. Bader, M. Tichy, C. A. Helm, R. Hippler, *Thin Solid Films* **2014**, *550*, 389.

[67] B. Abdallah, M. Naddaf, M. A-Kharroub, *Nucl. Instruments Methods Phys. Res. Sect. B Beam Interact. with Mater. Atoms* **2013**, *298*, 55.

[68] W. C. Oliver, G. M. Pharr, *J. Mater. Res.* **1992**, *7*.

[69] P. Pearson, A. Cousins, *Assessment of corrosion inamine-based post-combustion capture of carbon dioxide systems*, Elsevier Ltd, **2016**.

[70] S. Mohan, S. S. Nair, A. V. Ajay, M. S. Senthil Saravanan, B. R. Vishnu, S. P. Sivapirakasam, M. Surianarayanan, *Mater. Today Proc.* **2019**, *27*, 2492.

[71] M. N. Alias, Localized Electrochemical Study on Corrosion Behavior of Nitride Thin Films, University of Rhode Island, **1994**.

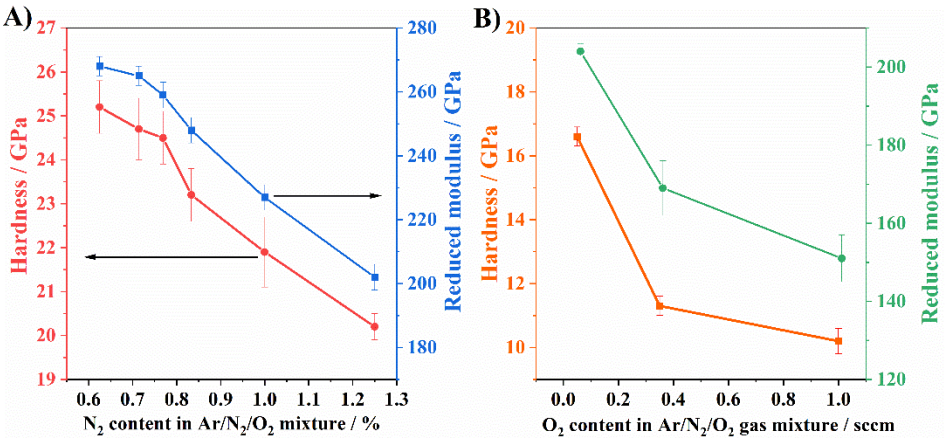

Figure 1. Hardness and reduced modulus of the A) Zr_xN_y and B) $Zr_xN_yO_z$ films prepared on Si substrates.

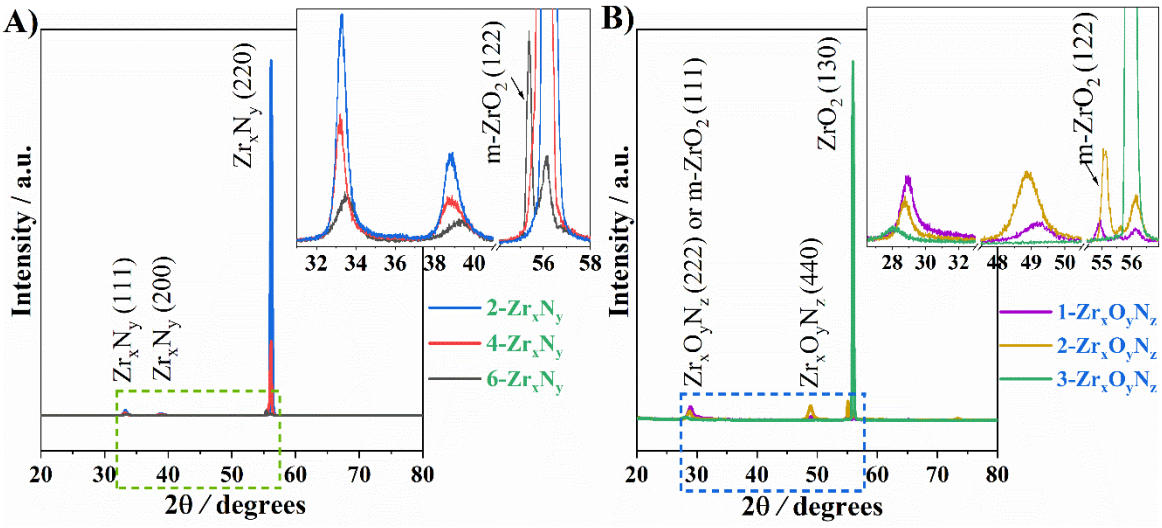

Figure 2. XRD spectra of the chosen A) Zr_xN_y films: 2-Zr_xN_y, 4-Zr_xN_y, and 6-Zr_xN_y, B) $Zr_xN_yO_z$ layers: 1-$Zr_xN_yO_z$, 2-$Zr_xN_yO_z$, and 3-$Zr_xN_yO_z$.

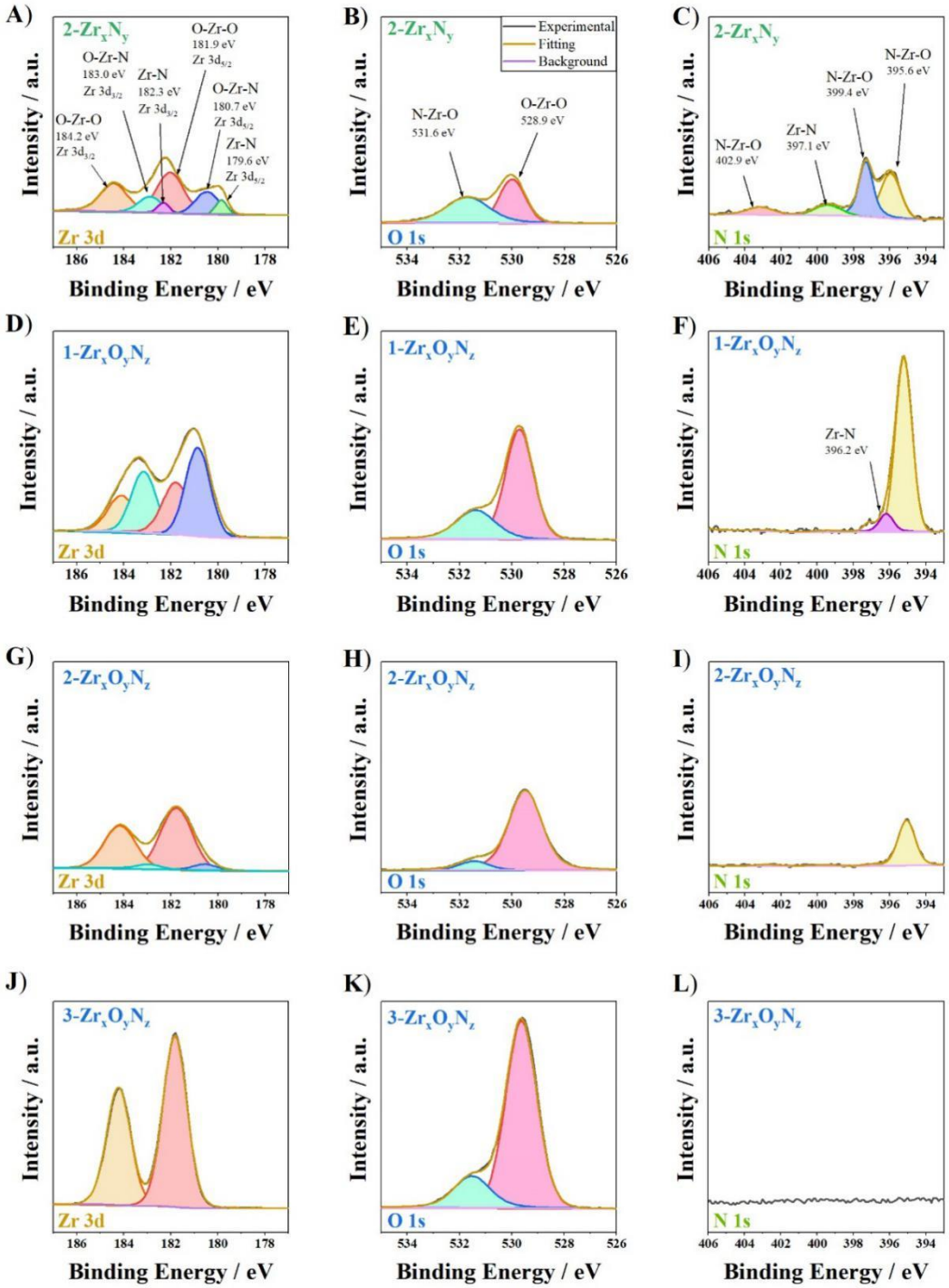

Figure 3. High-resolution XPS spectra of chosen samples: 2-Zr_xN_y signal of A) Zr 3d, B) O 1s, C) N 1s; 1-$Zr_xN_yO_z$ signal of D) Zr 3d, E) O 1s, F) N 1s; 2-$Zr_xN_yO_z$ signal of G) Zr 3d, H) O 1s, I) N 1s; 3-$Zr_xN_yO_z$ signal of J) Zr 3d, K) O 1s, L) N 1s.

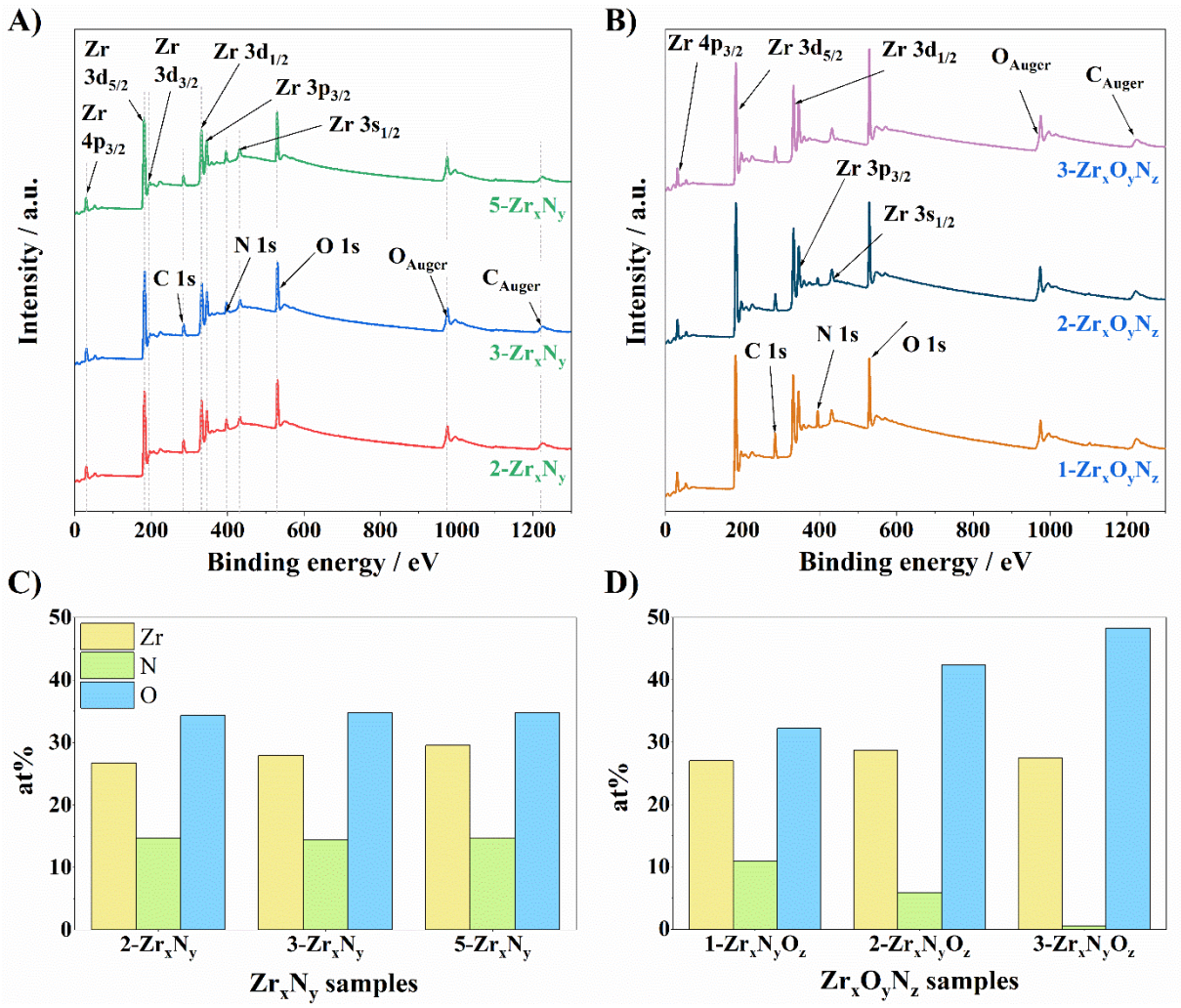

Figure 4. XPS survey scan of chosen (A) Zr_xN_y, and (B) $Zr_xN_yO_z$ samples; atomic concentration of oxygen, zirconium, and nitrogen in the chosen samples of (C) Zr_xN_y and (D) $Zr_xN_yO_z$.

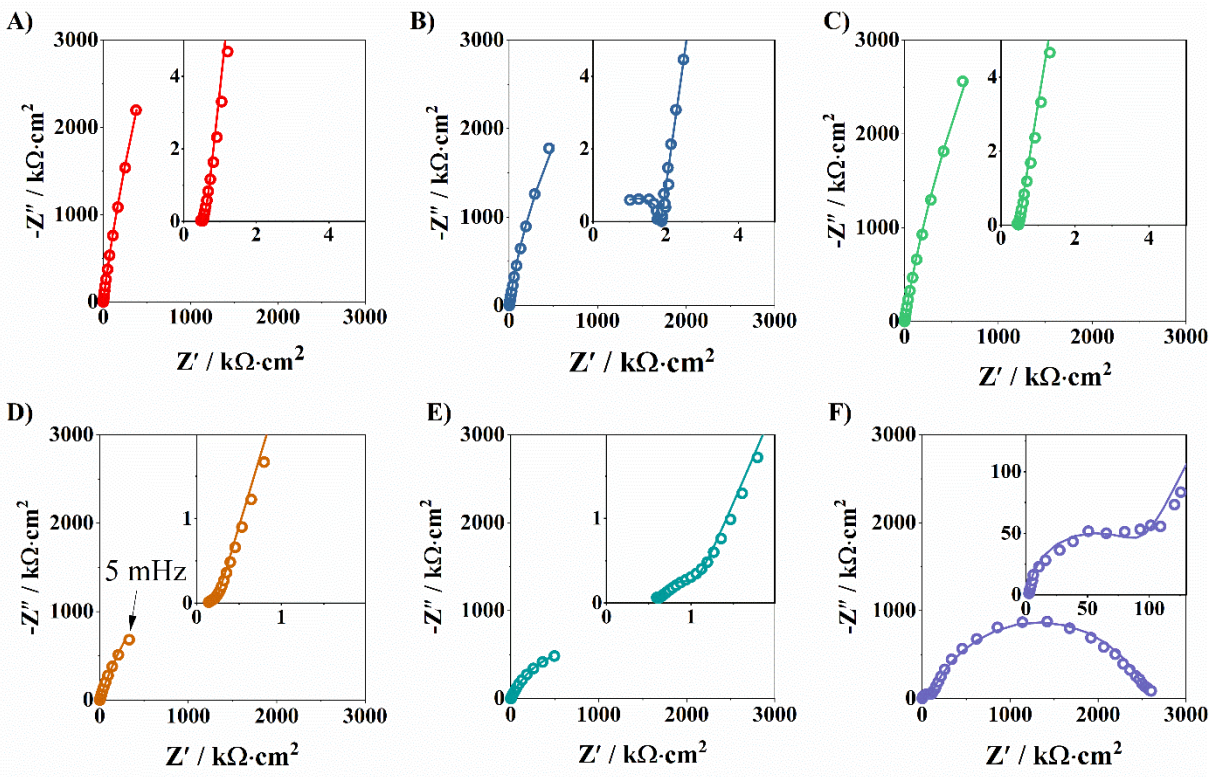

Figure 5. EIS impedance spectra in Nyquist representation recorded for chosen samples exposed to synthetic wastewater: A) 2-Zr_xN_y, B) 3-Zr_xN_y, C) 5-Zr_xN_y, D) 1-$Zr_xN_yO_z$, E) 2-$Zr_xN_yO_z$, F) 3-$Zr_xN_yO_z$.

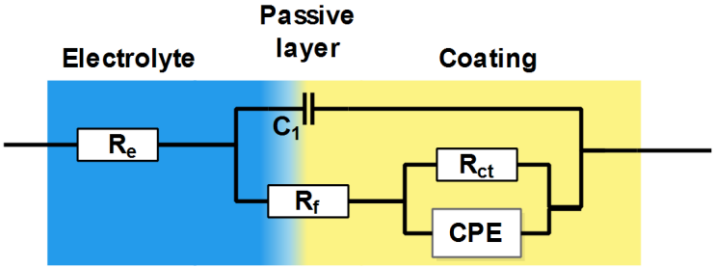

Figure 6. The electric equivalent circuit used for analysis, composed of two time constants, used for the fitting for all investigated layers.

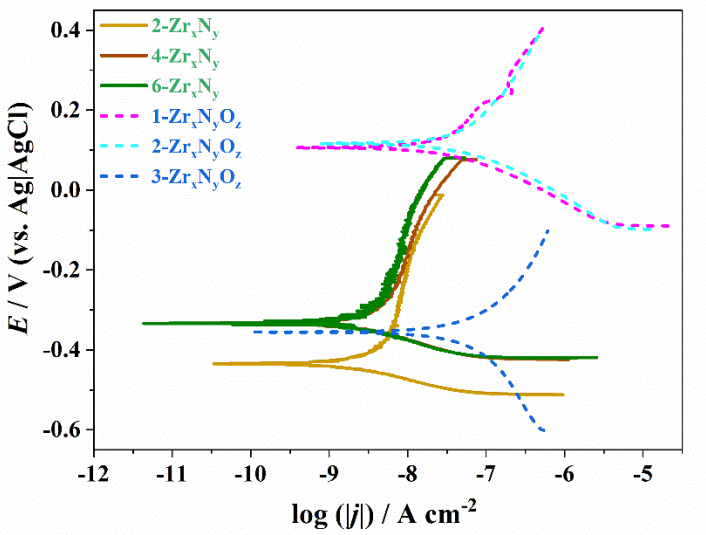

Figure 7. Linear polarization curves for the corrosion of chosen Zr_xN_y and $Zr_xN_yO_z$ layers in synthetic domestic wastewater.

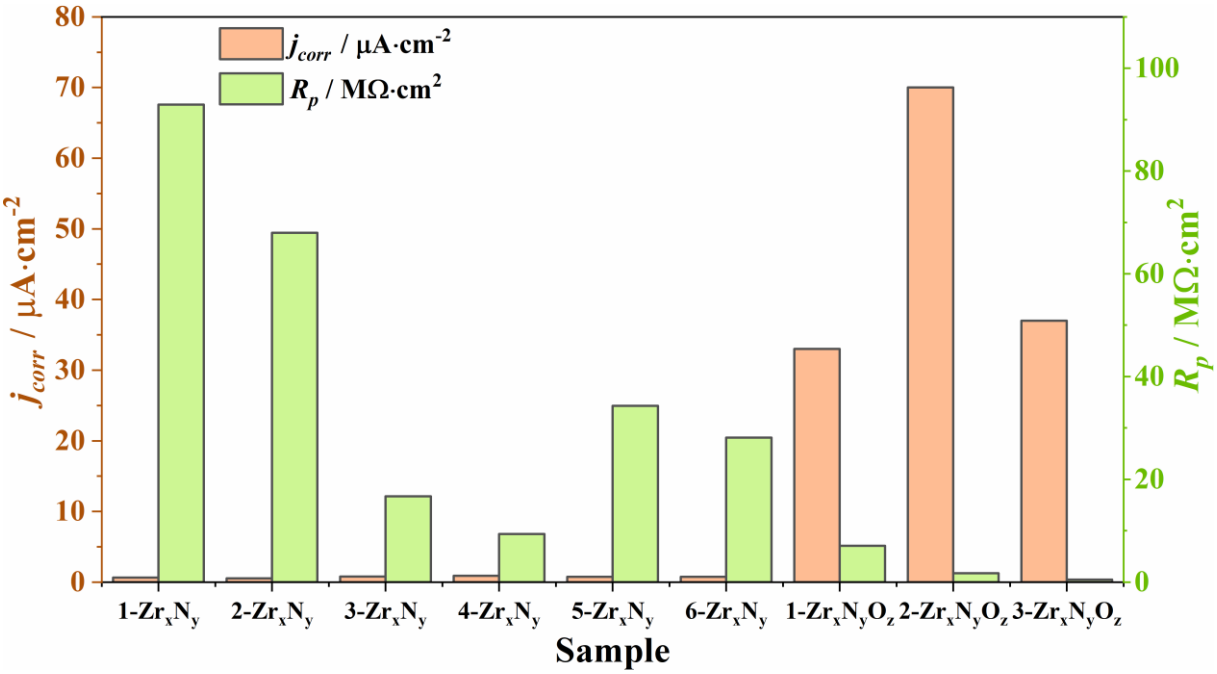

Figure 8. Comparison of the polarization resistance and corrosion current density (value estimated based on LP results) of Zr_xN_y and $Zr_xN_yO_z$ layers.

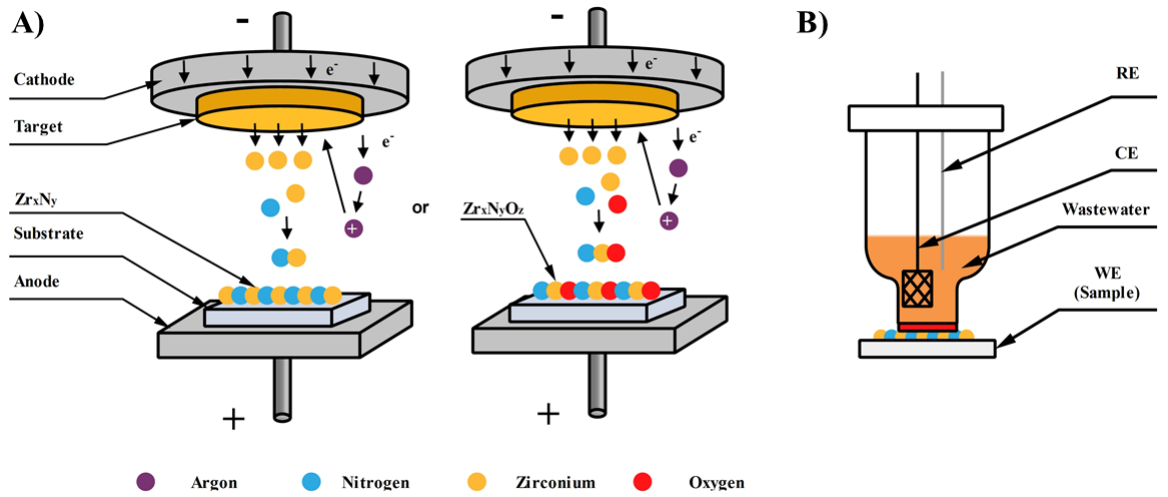

Figure 9. Zirconium nitride and oxynitride coatings for protective application: A) fabrication process by magnetron sputtering, B) configuration of electrochemical setup for corrosion studies.

Table 1. Resistance and thickness of chosen samples. Error of measured values is within 10%.

	Zr_xN_y						$Zr_xN_yO_z$		
	1-	**2-**	**3-**	**4-**	**5-**	**6-**	**1-**	**2-**	**3-**
Resistivity / Ω cm	17.8	6.0	2.9	2.6	2.3	1.8	$>10^6$	$>10^6$	$>10^6$
Thickness / nm	480	405	575	750	820	700	610	600	176

Table 2. Curve fitting results of Zr 3d, N 1s and O 1s spectra of chosen zirconium nitride and oxynitride coatings.

		Atomic concentration / %						
	BE / eV	**2-** Zr_xN_y	**3-** Zr_xN_y	**5-** Zr_xN_y	**1-** ZrO_xN_y	**2-** ZrO_xN_y	**3-** ZrO_xN_y	**Assignment**
Zr	179.6 ± 0.3	2.4	3.8	5.1	1.2	-	-	Zr-N
$3d_{5/2}$	180.7 ± 0.3	7.4	7.8	8.1	15.6	2.7	-	O-Zr-N

	181.9 ± 0.1	16.9	16.3	16.3	10.2	26	27.4	Zr-O
O 1s	529.8 ± 0.2	16.3	18.6	20.6	23.1	38.9	39.6	O-Zr-O
	531.6 ± 0.2	18	16.1	14.1	9.1	3.5	8.7	N-Zr-O
	395.6 ± 0.4	5.6	5.2	5.1	9.5	5	-	N-Zr-O
	396.2 ± 0.2	-	-	-	0.9	-	-	Zr-N
N 1s	397.1 ± 0.3	5.8	6.4	6.9	-	-	-	Zr-N
	399.4 ± 0.2	1.7	1.4	1.5	-	-	-	N-Zr-O
	402.9 ± 0.2	1.6	1.4	1.1	-	-	-	N-Zr-O

Table 3. Selected parameters calculated from the electrical equivalent circuit of the impedance spectra of zirconium nitride and zirconium oxynitride hard-coatings.

	1- Zr_xN_y	2- Zr_xN_y	3- Zr_xN_y	4- Zr_xN_y	5- Zr_xN_y	6- Zr_xN_y	1- $Zr_xN_yO_z$	2- $Zr_xN_yO_z$	3- $Zr_xN_yO_z$
C_1 / µF cm^{-2}	2.9	3.8	0.002	0.03	0.03	3.6	0.5	0.2	0.007
R_f / kΩ cm^2	1.2	0.7	1.5	0.1	0.1	0.7	0.1	0.5	18.7
R_{ct} / MΩ cm^2	34.9	68.0	16.7	9.4	34.3	28.1	7.1	1.7	0.5
Q_3 / µF·s$^{(n-1)}$cm^{-2}	4.4	5.6	10.5	9.7	7.1	5.6	21.8	15.1	0.6
n_3 / -	0.90	0.88	0.91	0.91	0.90	0.87	0.81	0.74	0.77
j_{corr} / nA cm^{-2}	0.7	0.4	0.2	0.3	0.8	0.9	3.6	150	52

Table 4. Electrochemical corrosion properties during exposure to synthetic domestic sewage obtained by fitting of linear polarization of zirconium nitride and oxynitride coatings.

	1- Zr_xN_y	2- Zr_xN_y	3- Zr_xN_y	4- Zr_xN_y	5- Zr_xN_y	6- Zr_xN_y	1- $Zr_xN_yO_z$	2- $Zr_xN_yO_z$	3- $Zr_xN_yO_z$
j_{corr} / µA cm^{-2}	0.7	0.5	0.8	0.9	0.8	0.8	33	70	37
E_{corr} / V	-0.43	-0.41	-0.33	-0.32	-0.33	-0.35	0.11	0.12	-0.36
V_{corr} / nm y^{-1}	80	64	95	111	92	92	4011	8507	4497

Table 5. Sample codification and deposition conditions.

	Sample code	Ar / sccm	N_2 / sccm	O_2 / sccm	Nitrogen content in $Ar/N_2/O_2$ mixture / %	Oxygen content in $Ar/N_2/O_2$ mixture / %
Zr_xN_y	1-Zr_xN_y	**40**			1.25	
	2-Zr_xN_y	**50**			1.00	
	3-Zr_xN_y	**60**			0.83	
	4-Zr_xN_y	**65**		-	0.77	-
	5-Zr_xN_y	**70**	0.5		0.71	
	6-Zr_xN_y	**80**			0.61	
$Zr_xN_yO_z$	1-$Zr_xN_yO_z$	50		**0.05**	0.99	0.10
	2-$Zr_xN_yO_z$			**0.35**	0.98	0.69
	3-$Zr_xN_yO_z$			**1.00**	0.97	1.94

The table of contents

Zr_xN_y and $Zr_xN_yO_z$ coatings are prepared by high-power impulse magnetron sputtering and investigated as potential corrosion-inhibiting coatings for the partial protection of advanced electrodes *e.g.*, in bioelectrochemical systems for electricity generation. The influence of the nitrogen content in the coatings on the electrochemical properties and corrosion resistance were investigated.

A. Dettlaff*, M. Brodowski, M. Kowalski, V. Stranak, V. Prysiazhnyi, E. Klugmann-Radziemska, J. Ryl, R. Bogdanowicz

Highly-oriented zirconium nitride and oxynitride coatings deposited via high-power impulse magnetron sputtering: crystal-facet driven corrosion behavior in domestic wastewater

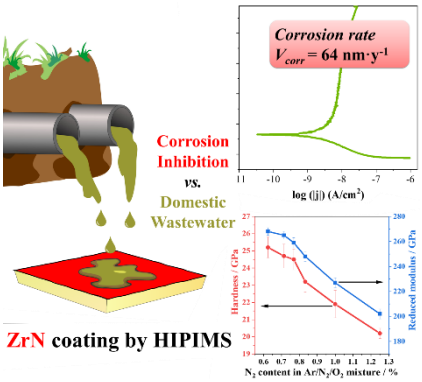

Supporting Information

Highly-oriented zirconium nitride and oxynitride coatings deposited via high-power impulse magnetron sputtering: crystal-facet driven corrosion behavior in domestic wastewater

Dr. Anna Dettlaff, Mateusz Brodowski, Marcin Kowalski, Prof. Vitezslav Stranak, Dr. Vadym Prysiazhnyi, Prof. Ewa Klugmann-Radziemska, Prof. Jacek Ryl, Prof. Robert Bogdanowicz*

Table S1. The composition of synthetic domestic wastewater.

Component	**Concentration / mg L^{-1}**
Pepton	114.0
Starch	38.0
Glucose	38.0
Glycerol	55.4
Ammonium acetate	122.0
$(NH_4)_2CO_3$	140.0
KH_2PO_4	9.0
NaH_2PO_4	10.0

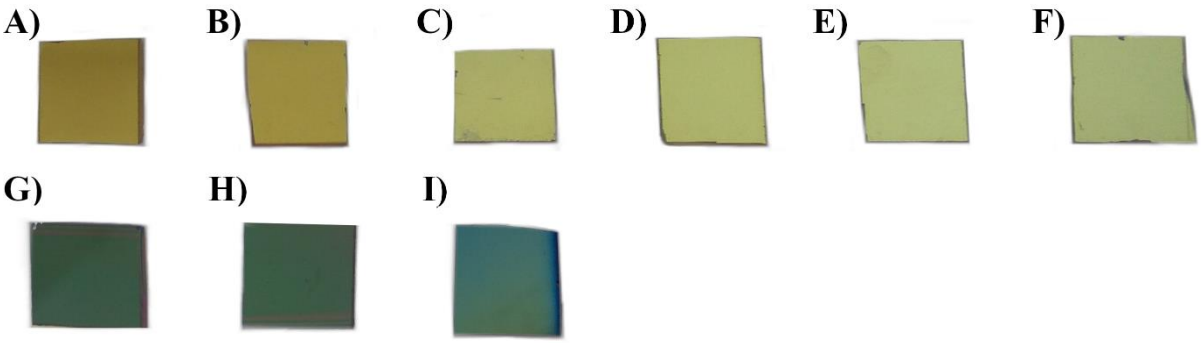

Figure S1. Image of A) 1-Zr_xN_y, B) 2-Zr_xN_y, C) 3-Zr_xN_y, D) 4-Zr_xN_y, E) 5-Zr_xN_y, F) 6-Zr_xN_y, G) 1-$Zr_xN_yO_z$, H) 2-$Zr_xN_yO_z$, I) 3-$Zr_xN_yO_z$ films.

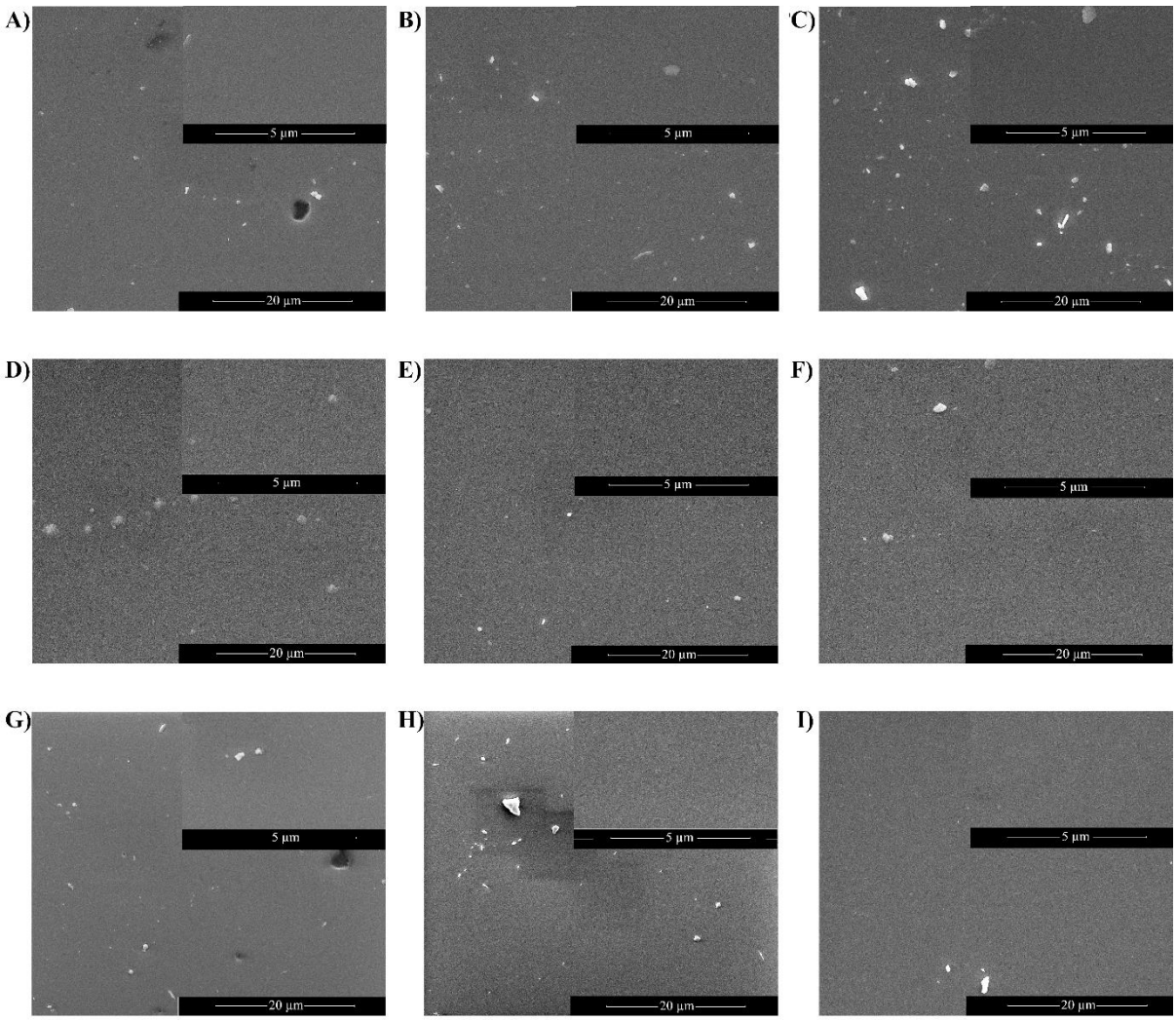

Figure S2. SEM images at magnification: x2 500 and insets x10 000: A) 1-Zr_xN_y, B) 2-Zr_xN_y, C) 3-Zr_xN_y, D) 4-Zr_xN_y, E) 5-Zr_xN_y, F) 6-Zr_xN_y, G) 1-$Zr_xN_yO_z$, H) 2-$Zr_xN_yO_z$, I) 3-$Zr_xN_yO_z$ films.

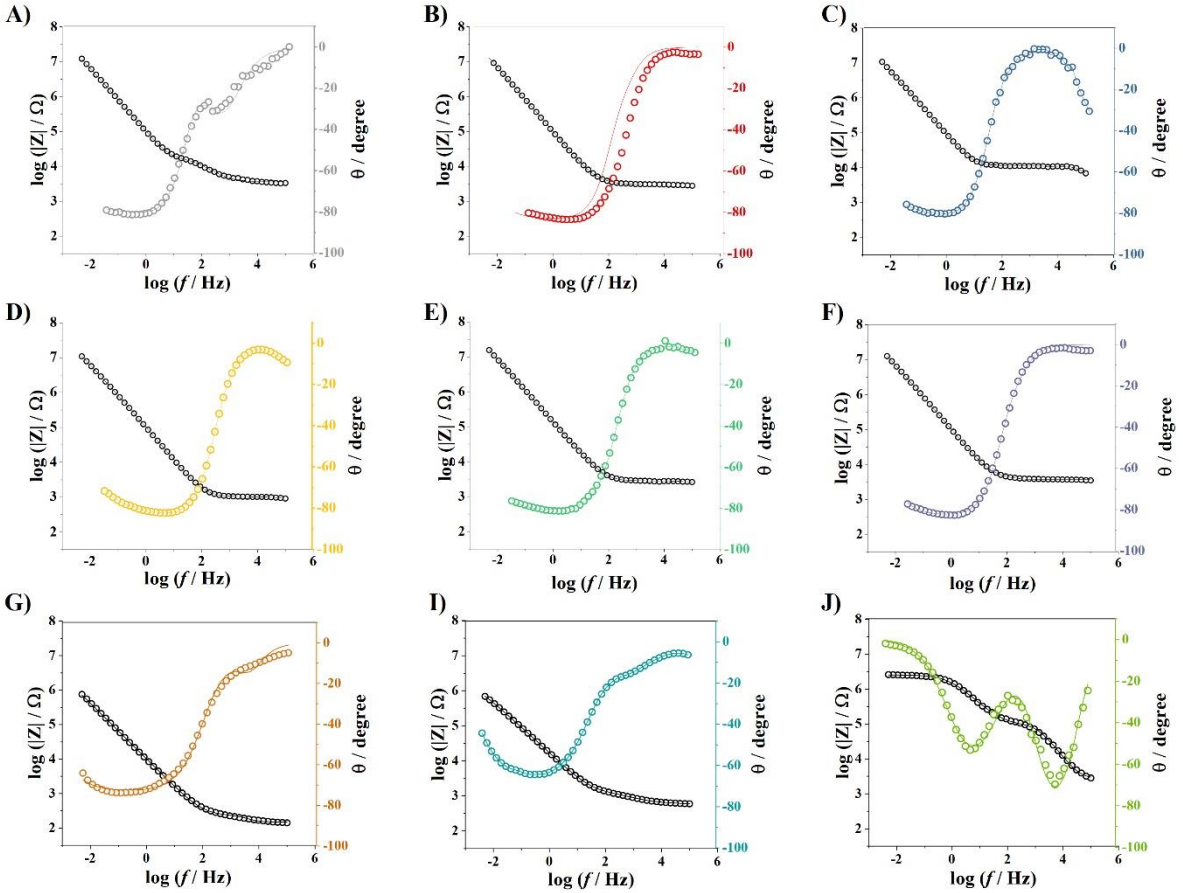

Figure S3. EIS impedance spectra in Bode representation recorded for different Zr_xN_y samples exposed to synthetic wastewater: A) 1-Zr_xN_y, B) 2-Zr_xN_y, C) 3-Zr_xN_y, D) 4-Zr_xN_y, E) 5-Zr_xN_y, F) 6-Zr_xN_y, G) 1-$Zr_xN_yO_z$, H) 2-$Zr_xN_yO_z$, I) 3-$Zr_xN_yO_z$ films.